Measuring Segment Piston with a Dispersed Fringe Sensor on the Giant Magellan Telescope

Marcos A. van Dam,[a] Brian A. McLeod[b] and Antonin H. Bouchez[c]

[a]Flat Wavefronts, 21 Lascelles Street, Christchurch 8022, New Zealand;
[b]Smithsonian Astrophysical Observatory, 60 Garden St., Cambridge, MA 02138, USA;
[c]Giant Magellan Telescope Observatory Corporation, P.O. Box 90933, Pasadena, CA 91109, USA

ABSTRACT

The Giant Magellan Telescope (GMT) consists of seven 8.365 m segments with a separation of 0.345 m. A unique challenge for GMT lies in phasing these segments and, in particular, how to measure segment piston optically. Making segment piston measurements is relatively straight-forward when using diffraction-limited light, such as wavefront-corrected light at near infrared wavelengths. Unfortunately, we don't have that luxury, since all of that light is passed to the science instrument. Instead, we must use stars 6'-10' from the optical axis when guiding with laser guide stars. The segment piston measurement can be made in two different ways using subapertures that span adjacent segments with dispersed broadband light. The Dispersed Hartmann Sensor takes the averages the Fourier phase of the dispersed fringes over baselines spanning the segment gap, while the Dispersed Fringe Sensor works by measuring the angle of the dispersed fringes. We explore the properties of the two approaches, discuss their relative advantages, and evaluate their performance using end-to-end simulations in YAO.

Keywords: phasing, Giant Magellan Telescope, adaptive optics, simulations

1. INTRODUCTION

The Giant Magellan Telescope (GMT) consists of seven 8.365 m circular segments with a separation of 8.710 m between the central segment and the outer segments. The GMT is a Gregorian design with an adaptive secondary mirror (ASM). The ASM is also segmented, with the segments critically sized with respect to the primary mirror segments. The design of the GMT is ideal for ground-layer adaptive optics, high contrast imaging and imaging at thermal infrared wavelengths.

In order to image at the diffraction limit of the telescope (equivalent to a diameter of approximately 25.4 m), it is crucial to phase the primary and secondary mirrors to a fraction of the imaging wavelength. There are two planned diffraction-limited adaptive optics (AO) modes for the GMT, which require a phased telescope.[1] A natural guide star adaptive optics (NGS AO) system with a visible light pyramid wavefront sensor is used when there is a sufficiently bright star near the science target. For greater sky coverage, there is also a laser tomography adaptive optics (LTAO) system that employs six side-projected laser guide stars, along with a single natural guide star to measure tip-tilt. This tip-tilt star can be much fainter and further away from the science target than the star used NGS AO. In addition, it is envisioned that most other observations will benefit from correction using the ground-layer adaptive optics (GLAO) mode. For GLAO at visible wavelengths, phasing the telescope does not significantly improve the performance.

A phasing sensor is needed to make segment piston measurements while the telescope is used for science. The phase measurements will be made using the Acquisition, Guiding and Wavefront Sensor (AGWS) system. This consists of four off-axis units that operate between $6'$ and $10'$ from the optical axis. Each AGWS also has a visible light wavefront sensor to measure position errors and distortions in the optical figure of the primary and secondary mirrors, as well as turbulence near the ground when operating in GLAO mode.

In this paper, we consider the challenge of measuring segment piston using off-axis starlight. Any segment tip-tilt in the primary mirror (optically conjugate to the ground) that is compensated by the ASM (optically

Further author information: send correspondence to Marcos van Dam, marcos@flatwavefronts.com

conjugate to 165 m) will induce an off-axis segment piston error. As a result, a minimum of three off-axis measurements are needed to solve for the ambiguity between segment piston and segment tip-tilt.

The problem of phasing telescopes with tessellated hexagonal segments, such as the telescopes at the W. M. Keck Observatory, has been well studied and phase sensors have been successfully implemented.[2,3] At the W. M. Keck Observatory, the segment gaps are of the order of 3 mm and even visible light has excellent coherence across the segment gap. By contrast, the GMT has a minimum gap of 350 mm, which leads to greatly reduced coherence of light across subapertures that span the segment gap.

The phasing sensor is a crucial part of the overall phasing strategy of the telescope, which is explained in detail elsewhere.[4] The optical segment piston sensors for GMT are required to measure segment piston to an accuracy of 50 nm or better once every 30 s. The sky coverage requirement is over 90% of the sky near the South Galactic Pole. The sensor must have a capture range of at least 50 µm, which is the accuracy of the laser tracker metrology system.

The original concept proposed by Codona to phase the GMT was a Hartmann sensor that spans each pair of neighboring segments as shown in Fig. 1.[5] There are 12 square subapertures in the phasing sensor, with the

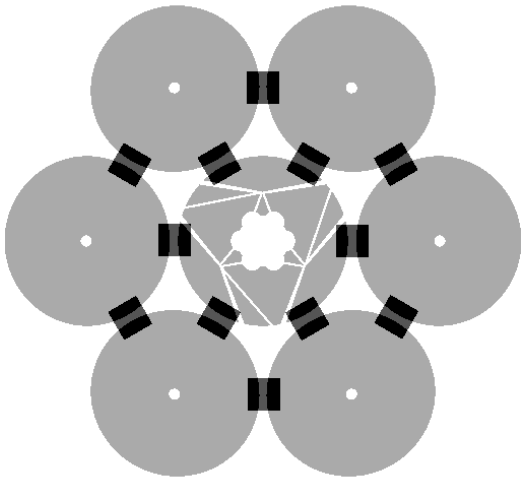

Figure 1: Pupil with the location of the 12 subapertures.

length and width equal to 1.5 m. The location of the subapertures is chosen so that they are centered on the inter-segment gap. The secondary mirror is critically sized with respect to the primary mirror, so the pupil is vignetted horizontally when operating off-axis. This leads to an increase in the effective size of the segment gap for the DFS, which operates 6′ and 10′ off-axis.

The location of the subapertures is adjusted to reflect the change in the telescope pupil as a function of location in the field. The shift in subaperture location can be implemented by conjugating the lenslet array to an altitude half-way between the conjugate altitudes of the primary and secondary mirrors. An example of how the pupil and subaperture location change with off-axis distance is shown in Fig. 2

2. HARTMANN SENSOR

In Codona's concept, 30 s tip-tilt corrected images at K-short are captured. At the time, eAPD arrays that are capable of taking short-exposure images with subelectron noise were not yet conceived. In the work presented here, we use short exposure images and recenter them digitally. Each subaperture produces an image like the one presented in Fig. 3. The center of the images is found using an iterative centroid algorithm, and the images are recentered by applying a linear phase in the Fourier domain. 3000 consecutive frames of 10 millisecond exposures are coadded to obtain an estimate based on 30 seconds of data.

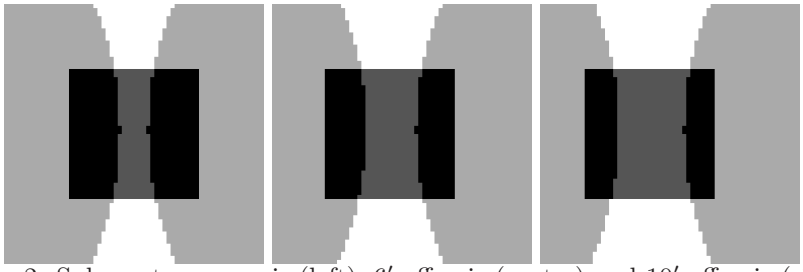

Figure 2: Subaperture on-axis (left), 6′ off-axis (center) and 10′ off-axis (right).

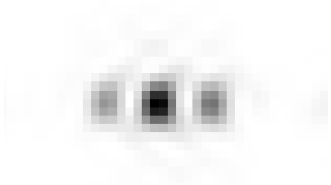

Figure 3: Undispersed image with piston but no turbulence.

The segment piston is estimated from the Fourier phase of the images as follows. Let us denote the area within a subaperture on one side of the segment gap as p_A and the area on the other side as p_B. The aim of the piston sensor is to estimate the difference in mean phase between one side and the other:

$$\Delta\phi = \int \phi(p_A) - \int \phi(p_B). \tag{1}$$

First, a weighting function, O_{AB} is defined as:

$$O_{AB} = \mathrm{F}^{-1}\{\mathrm{F}\{p_A\}\mathrm{F}\{p_B\}^*\}, \tag{2}$$

where F{} is the Fourier transform operator and * denotes the complex conjugate. For each image, I, we obtain the estimate of the phase difference using the relationship

$$\Delta\phi = \int |O_{AB}|\arg(O_{AB}\mathrm{F}\{I\}), \tag{3}$$

where arg is defined as

$$\arg(\mathrm{x}) = \mathrm{atan}(\Im(\mathrm{x}), \Re(\mathrm{x})). \tag{4}$$

This is shown pictorially in Fig. 4.

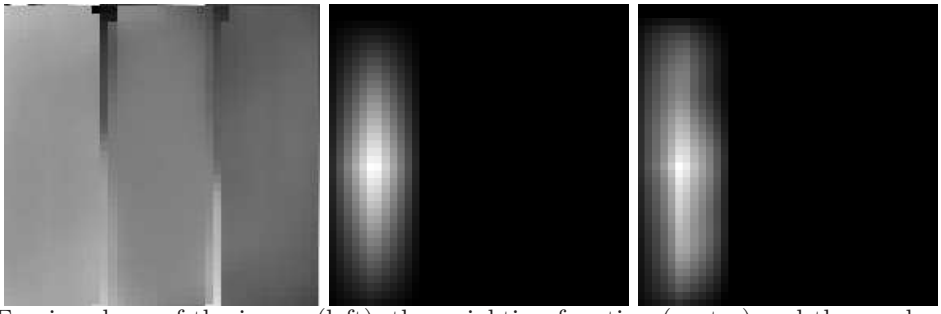

Figure 4: The Fourier phase of the image (left), the weighting function (center) and the product of the Fourier phase and the weighting function (right). The phase difference is obtained by integrating the image on the right.

The Hartmann sensor is an interferometric measurement that requires good coherence across the segment gap. Tip-tilt stabilization of each subaperture and long wavelengths are needed to combat the effects of atmospheric turbulence. This sensor has been validated on the Magellan Clay telescope.[6]

The main limitation of the Hartmann sensor is that the capture range is limited to half a wave (about 1 µm at K-band). An excellent way to increase the capture range by dispersing the fringes is explained in Section 3.

3. DISPERSED FRINGE SENSOR

The dispersed fringe sensor (DFS) has been proposed as technique to provide coarse sensing of the segment piston of the James Webb Space Telescope and has been extensively tested in the lab and on the sky at W. M. Keck Observatory.[7,8] In this paper, we propose a new way to analyze the signal using short exposures that freeze the blurring due to atmospheric turbulence. Numerical simulations show that this sensor is able to meet the GMT requirements.

The DFS presented in this paper uses the same subapertures as the Hartmann sensor but disperses the light in the direction parallel to the segment gap using a grism.

The parameters used in the simulations are summarized in Table 1.

Table 1: **DFS parameters used in the simulations. The pixel extent is slightly smaller than Nyquist sampling at the shortest wavelength of the passband.**

Subaperture length (L)	Dispersion	Pixel angular extent
1.5 m	$6.67''\,\mu\text{m}^{-1}$	$0.4\lambda_{\text{min}}/L$ rad

The DFS is located at the Gregorian focus of the GMT on the instrument rotator. Its optical design can be summarized as follows. The converging beam reflects off a pickoff mirror, approaches the focus and passes through a K-mirror to derotate the pupil orientation. Then the beam is collimated to form a pupil image. At the pupil, a laser-cut aperture mask is placed, followed by a hexagonal grid lens array to form separate images from each subaperture and an array of grisms to disperse the light. After the focus of the lens array, the beam is reimaged into an infrared camera with another relay.

The signal processing used to retrieve the segment piston is very different to that found in the literature. Shi matches the observed fringes to a template,[7] while Albanese takes cross sections of the fringes and extracts the magnitude and locations of the peaks.[8] Neither of these methods is applicable to the GMT, where the segment gaps are large. Instead, we use a very simple but effective procedure that relies on the fact that a segment piston error causes a shear in the fringes, as can be seen in Fig. 5.

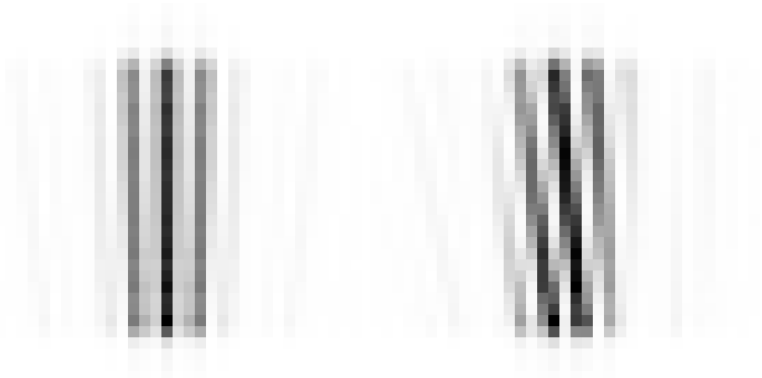

Figure 5: Dispersed fringes at J-band corresponding to no segment piston (left) and 5 microns of segment piston (right).

If we take the Fourier transform of the fringes in Fig. 5, we find that the y-ordinate of the location of the side lobes changes linearly with segment piston, as shown in Fig. 6. By finding the location of the peak of one of the side lobes, we obtain an estimate of the segment piston. The theory explaining how segment piston appears in the signal is explained elsewhere.[9]

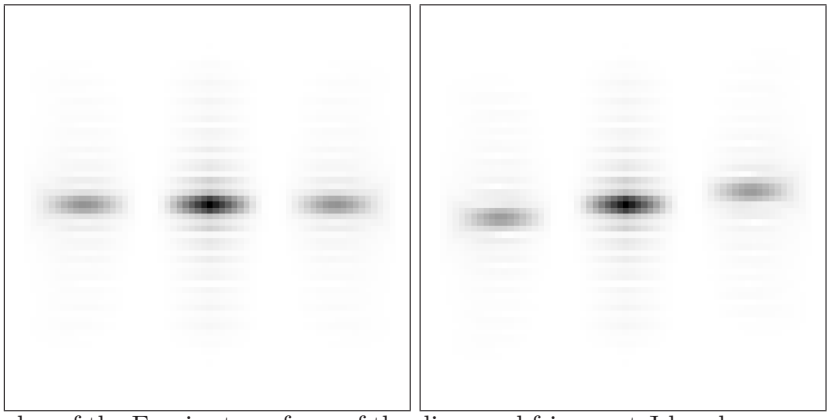

Figure 6: Absolute value of the Fourier transform of the dispersed fringes at J-band corresponding to no segment piston (left) and 5 microns of segment piston (right).

The linearity of the signal with applied segment piston is excellent. The proportionality factor depends on the geometry of the pupil on the subaperture, the spectral distribution of the light and the dispersion of the grism. The 12×7 interaction matrix, M, describes how the location of the peak changes for each of the 12 subapertures when each of the seven segments is poked. It is calculated by poking the segments one at a time and measuring the change in the location of the peak. Due to the large linear range, we can use large segment pokes (*e.g.*, 5 µm), so this calibration can be performed using star light as well as with a calibration source. The reconstructor, M^+, used to convert the DFS measurements into segment piston commands, is the regularized pseudo-inverse of M:[10]

$$M^+ = (M^T M + \alpha I + \beta)^{-1} M^T, \tag{5}$$

where α is a small regularization constant, I is the identity matrix and β is a large constant used to penalize global piston.

The calibration zero point (*i.e.*, the location of the peak where the segments are in phase) depends only on the angle between the grism and the detector, but not on the subaperture illumination. As a result, the zero point of the DFS can be calibrated with a light source that does not pass through the telescope.

The exposure time needs to be set shorter than the atmospheric decorrelation time in order to restrict the blurring of the fringes. A typical J-band instantaneous exposure imaged through atmospheric turbulence is shown in Figure 7. An instantaneous tip-tilt across the subaperture has displaced the image to the right. Fortunately,

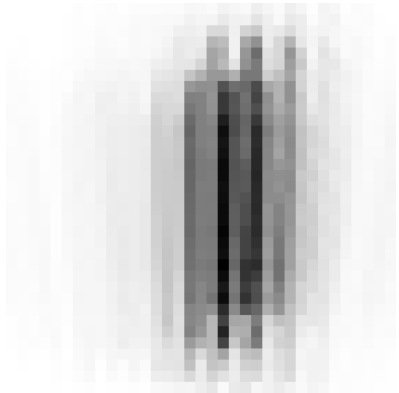

Figure 7: J-band fringe imaged through turbulence with an r_0 value of 0.13 m.

this has no effect on the segment piston estimate, because the absolute value of the Fourier transform is not affected by image shifts. However, tip-tilt at a high temporal frequency can blur the short exposure images.

When imaging through turbulence, the short exposures are processed by taking the absolute value of the Fourier transform and coadding this quantity. The reason short exposures are needed can be seen graphically in Fig. 8, where the absolute value of the Fourier transform of the fringes as a function of exposure time is displayed. In Fig. 8, the total integration time is 1 s. For example, for the case of 10 ms exposures, we coadd the absolute value of the Fourier transform of 100 consecutive frames. The fringe contrast starts to degrade for exposure times longer than 10 ms at J-band.

At shorter wavelengths, shorter exposures are needed to optimize the fringe contrast, while for longer wavelengths, the exposure time can be increased without loss of performance. In this paper, we use 3000 consecutive 10 ms frames to obtain an estimate of the segment piston once every 30 s. The optimal exposure time depends on the guide star magnitude and the spectral filter, but, unless otherwise stated, a 10 ms exposure time is used for simplicity.

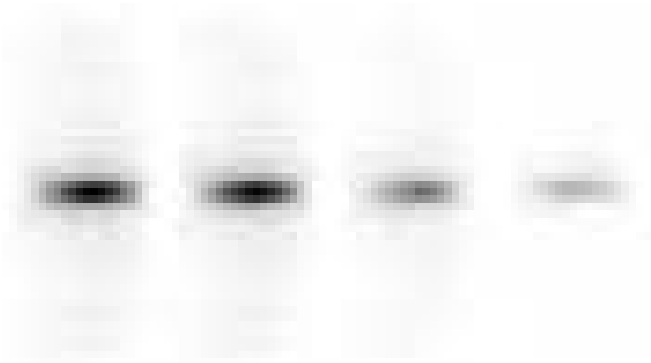

Figure 8: Absolute value of the Fourier transform of the fringes as a function of exposure time: from left to right, 1 ms, 10 ms, 100 ms, 1000 ms using a total integation of 1 s. Only one of the side lobes is shown. This simulation used J-band imaging through turbulence with an r_0 value of 0.13 m.

4. SIMULATION DESCRIPTION

4.1 Simulation tool

Numerical simulations were run to optimize the operating parameters of the DFS and to determine the performance and the sky coverage. The simulations presented in this paper were run in YAO (Yorick Adaptive Optics).[11] YAO is a general purpose, Monte Carlo adaptive optics simulation tool written in the Yorick language by Francois Rigaut with numerous contributions from the community. YAO has previously been used to simulate all of the adaptive optics modes for the GMT.[12–14] Some new YAO modules were written in support of this work. A pupil generation code was written that calculates how the GMT pupil varies as a function of guide star location. In addition, a new wavefront sensing module, which is described below, was written to simulate the DFS.

The square subapertures are centered to span the segments at a location where the segment gaps are as small as possible. The subapertures are rotated to be parallel to the segment gap. Broadband light is modeled using 16 equally spaced discrete wavelengths. The pixel scale is constant for all wavelengths within a spectral filter, so the zero-padding in the pupil plane varies accordingly. The dispersion, is simulated by adding wavelength dependent tip-tilt parallel to the segment gap. The monochromatic images are then added together to produce a single polychomatic image representative of broadband light.

The DFS is run behind a generic adaptive optics system providing closed-loop correction of the on-axis atmospheric turbulence. The AO system was modeled as being a 50×50 ideal Shack-Hartmann WFS with 51×51 actuators in a regular grid. The AO system produces an on-axis K-band Strehl ratio of 0.6 when there is no telescope segment piston, corresponding to an RMS wavefront error of about 250 nm. Note that because the DFS is far off-axis, so the AO correction actually degrades the DFS performance.

The applied telescope segment piston error in the simulations, with an RMS wavefront value of 300 nm, is shown in Fig. 9.

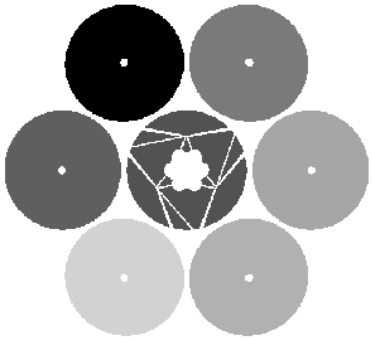

Figure 9: Segment piston error used in the simulations. The RMS value of the segment piston is 300 nm.

4.2 Atmospheric parameters

The turbulence profile used in the simulations that follow are profiles for Las Campanas Observatory from January 2008 with typical ground-layer and typical free-atmosphere turbulence.[15] This turbulence profile is reproduced in Table 2 for convenience. Since the requirements were written for 75$^{\text{th}}$ percentile seeing, the strength of every layer was increased to make the value of r_0 equal to 0.13 m at 500 nm. An outer scale of 30 m is used in the simulations. The science target is assumed to be at zenith.

Table 2: **Turbulence profile used in the simulations**

Height	Turb. fraction	Wind speed	Wind direction
25 m	0.126	5.65 m s^{-1}	0.78°
275 m	0.087	5.80 m s^{-1}	8.25°
425 m	0.067	5.89 m s^{-1}	12.48°
1250 m	0.350	6.64 m s^{-1}	32.50°
4000 m	0.227	13.29 m s^{-1}	72.10°
8000 m	0.068	34.83 m s^{-1}	93.20°
13 000 m	0.075	29.42 m s^{-1}	100.05°

4.3 Photometric and noise parameters

Table 3: **Photometry and noise parameters used in the simulations. The photometric zero point is for the whole telescope on-axis. The background at K-short depends on the off-axis distance, as explained in the text.**

Parameter	I-band	J-band	H-band	K-short
Central wavelength	0.79 µm	1.215 µm	1.654 µm	2.157 µm
Bandwidth	0.15 µm	0.26 µm	0.29 µm	0.32 µm
Photometric zero point	2.7×10^{12}	1.9×10^{12}	1.1×10^{12}	0.55×10^{12}
Background	16.3	16.3	13.7	12.1-12.6
Quantum efficiency	0.9	0.8	0.8	0.8
Optical throughput	0.38	0.46	0.46	0.46
Excess noise factor	1.41	1.35	1.35	1.35
Readout noise	0.4 e$^-$	0.4 e$^-$	0.4 e$^-$	0.4 e$^-$
Dark current	10 e$^- s^{-1}$	10 e$^- s^{-1}$	10 e$^- s^{-1}$	10 e$^- s^{-1}$

The filters used in the simulations are I-band, J-band, H-band and K-short, with central wavelengths of 0.79 µm, 1.215 µm, 1.654 µm and 2.157 µm respectively.

For I-band imaging, the detector is an electron multiplying charge coupled device (EMCCD) such as an OCAM2K camera from First Light Imaging. For the other bands, the detector is taken to be SAPHIRA, an infrared electron-initiated avalanche photodiode (e-APD) array produced by SELEX.[16] The existing SAPHIRA devices cannot operate at wavelengths shorter than 1.3 µm, but work is progressing on a device that can also operate at J-band. The dark current value is estimated from Atkinson *et al.* to be 10 $e^{-}s^{-1}$.[17]

The sky background at I-band corresponds to the pessimistic case of pointing the telescope 40° from the full moon. Calculating the background at K-short is complicated, since the background is the sum of photons emanating from the sky and the emissive structure of the telescope. We assume that there is a cold stop with the same shape as the on-axis telescope pupil and conjugate to the primary mirror. As the off-axis distance increases, the fraction of the emissive structure of the telescope seen by the DFS increases and the total background correspondingly increases.

Other photometric parameters are derived from a GMT internal document titled "Photometry for AO Simulations".[18] A summary of the parameters that affect the signal-to-noise ratio of the piston measurement is presented in Table 3.

5. PERFORMANCE OF DHS

In this section, we present simulation results using the dispersed version of the Hartmann sensor (DHS). As previously mentioned, dispersion is necessary to obtain the desired capture range.

5.1 Performance with varying turbulence strength

Noiseless simulations were run with a range of r_0 values. The results, plotted in Fig. 10, show that tip-tilt correction over the subaperture is essential. The DHS operates best at K-short, but could also work at H-band.

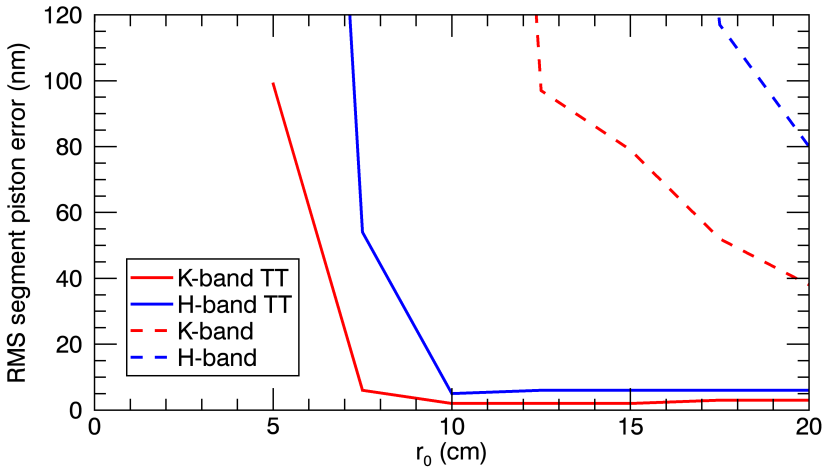

Figure 10: Performance as a function of r_0 at 500 nm for the at H-band and K-short, with and without tip-tilt correction.

Simulations were run to determine the limiting magnitude of a K-short DHS (Fig. 11). It can be seen that this sensor provides excellent sky coverage. In Fig. 11, squares are plotted at the locations where the probability of finding three or four guide stars of that magnitude at the South Galactic Pole is 95%. The y-ordinate for the squares has a value of 87 nm: this was chosen because three independent measurements with an error of 87 nm leads to an overall error of 50 nm.

The availability of the stars was computed using simulated star fields using the Besancon star model. Simulated star fields, rather than actual star fields, were used because they allow us to model star counts at any

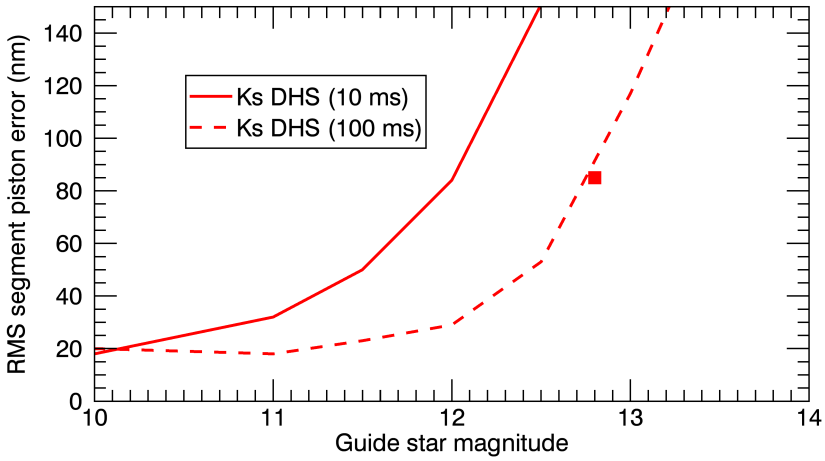

Figure 11: Performance as a function of guide star magnitude at K-short for two different exposure times. The square represents the minimum limiting magnitude needed to obtain 95% sky coverage at the South Galactic Pole.

wavelength to any limiting magnitude. Existing catalogs are much more restricted in terms of the specific filters and limiting magnitudes, especially at infrared wavelengths.

The Besancon web interface[19] was used to generate simulated catalogs of a region at the South Galactic Pole. A star field was deemed to be suitable if three or four stars brighter than the limiting magnitude can be acquired with the AGWS subject to the following constraints:

- Radial distance between 6′ and 10′
- Sensors can move ±60° in azimuth from their nominal azimuth position of 0°, 90°, 180° and 270°.
- Minimum azimuth distance of 40° between adjacent sensors.

The limiting magnitude as a function of desired sky coverage at the South Galactic Pole is tabulated in Table 4.

Table 4: **Limiting magnitude as a function of sky coverage at the South Galactic Pole.**

Sky coverage	50%	80%	90%	95%	99%
I-band	12.89	13.67	14.03	14.27	14.81
J-band	12.31	12.98	13.34	13.58	14.01
H-band	11.86	12.44	12.82	13.11	13.50
K-short	11.72	12.32	12.66	13.01	13.36

6. PERFORMANCE OF DFS

In this section, we present simulation results. Unless otherwise stated, the results correspond to a bright star at a location of [420′,0′], through turbulence with an r_0 of 0.13 m. The exposure time is set to 10 ms, except for the faintest stars at K-short, where we increase the exposure time 100 ms. In all cases, the absolute value of the Fourier transform of the short exposures is coadded to obtain one segment piston estimate every 30 s. In practice, segment piston could be estimated at a faster rate when bright stars are available.

6.1 Capture range

The requirement for the capture range of the segment piston sensor is 50 µm, which is the accuracy of the laser tracker metrology system. This means that if the telescope is phased except for a single segment which is displaced by 25 µm (leading to 50 µm of wavefront error), we can measure the segment piston sufficiently well that it can be driven to its correct position in three iterations. Smaller capture ranges could be accommodated by scanning the segments until they fall within the capture range, with a loss of observing efficiency. Simulations show that the maximum detectable piston wavefront error caused by a displaced segment is 30 µm at I-band, 40 µm at J-band, 60 µm at H-band and 100 µm at K-short. Only the H-band and K-short filters meet the requirements, but the other two are close enough to make a workable sensor.

6.2 Performance with varying turbulence strength

Noiseless simulations were run with a range of r_0 values. The results, plotted in Fig. 12, show that the DFS can operate in the observing conditions in which the LTAO and NGS AO systems will be used (typically $r_0 \geq 0.1$ m).

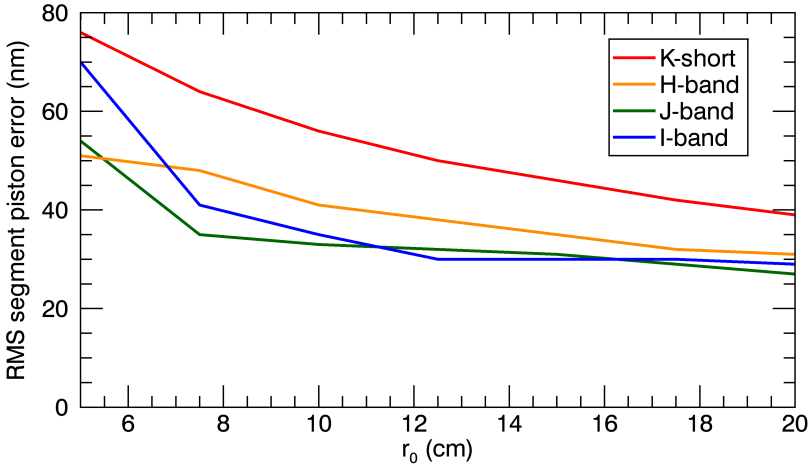

Figure 12: Performance as a function of r_0 at 500 nm for the four bands.

6.3 Limiting magnitude

Simulations were run with different magnitude stars to understand the limiting magnitude. The RMS segment piston error as a function of guide star magnitude is plotted in Fig. 13.

It can be seen that, according to this criterion, the 95% sky coverage is only attained at J-band.

Analytic calculations and full end-to-end simulations, plotted in Fig. 14, show that the 50 nm phasing error requirement can be achieved over 99% of the sky at the South Galactic Pole with a J-band DFS.

7. CONCLUSION

In this paper, we investigate the performance of the DFS for measuring segment piston on the GMT. A novel, simple but effective algorithm for estimating segment piston using short exposure images is presented. This involves taking the absolute value of the Fourier transform of a sequence of images and coadding them. The displacement in the location of the peak is proportional to a segment piston error.

We find that a J-band DFS, using a state-of-the-art SAPHIRA e-APD works best. It can operate through turbulence conditions with r_0 as small as 0.06 m, and can guide on stars as faint as $m_J = 13.6$. The resulting sky coverage at the South Galactic Pole is 90% for errors below 50 nm, and the telescope can still be well phased over 99% of the sky. In the unlikely case that SAPHIRA does not deliver the expected performance at J-band,

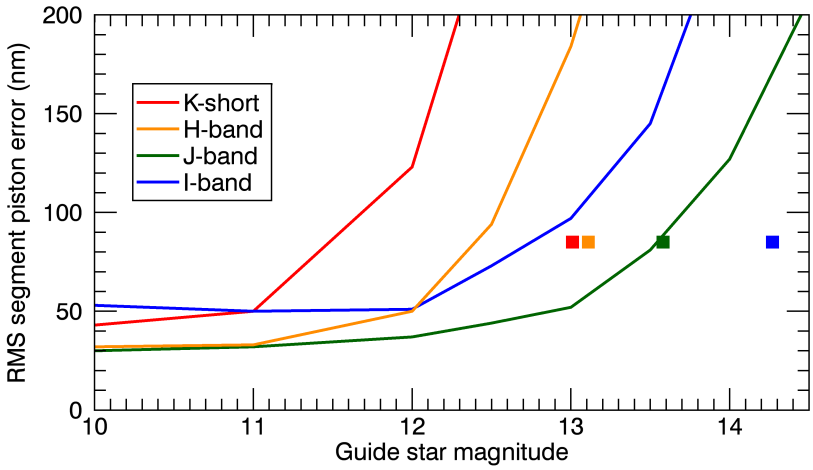

Figure 13: Performance as a function of guide star magnitude for three different spectral filters. The squares represent the minimum limiting magnitude needed to obtain 95% sky coverage at the South Galactic Pole.

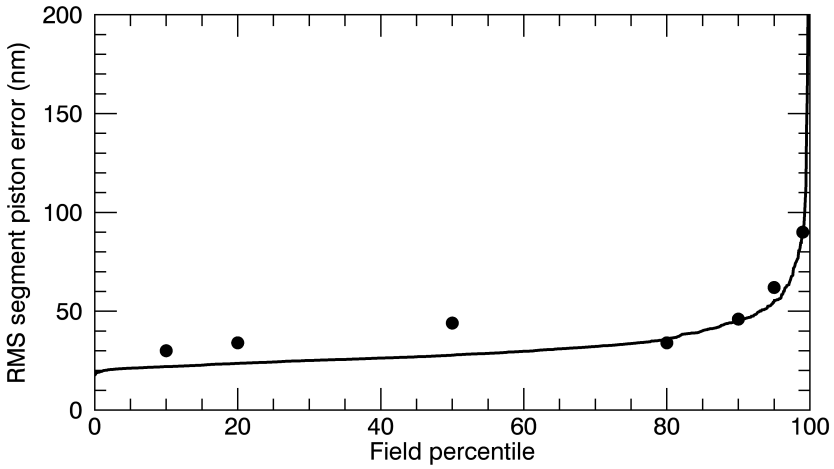

Figure 14: Calculated RMS segment piston error as a function of field percentile at the South Galactic Pole with a J-band DFS. The points represent the results from end-to-end simulations.

we could operate at H-band instead with a reduction in sky coverage. The capture range of 40 µm comes very close to the requirements.

There are two potential problems. When operating away from zenith, DAR will shear the fringes in a similar way to segment piston. As a result, care is needed to either measure or control the effect of DAR. When the wind-shake is strong, the effect of segment tip-tilt on the DFS could lead to unacceptable performance.

Overall, the DFS solution appears very promising and prototypes are under design for sky testing on existing telescopes.

Acknowledgments

This work has been supported by the GMTO Corporation, a non-profit organization operated on behalf of an international consortium of universities and institutions: Astronomy Australia Ltd, the Australian National University, the Carnegie Institution for Science, Harvard University, the Korea Astronomy and Space Science Institute, The Sao Paolo Research Foundation, the Smithsonian Institution, The University of Texas at Austin, Texas A&M University, University of Arizona and University of Chicago.

REFERENCES

[1] A. H. Bouchez *et al*, "The Giant Magellan telescope adaptive optics program," Proc. SPIE **9148**, 91480W (2014).

[2] G. Chanan *et al.*, "Phasing the mirror segments of the Keck telescopes: the broadband phasing algorithm," Appl. Opt. **37** 140-155 (1998).

[3] G. Chanan *et al.*, "Phasing the mirror segments of the Keck telescopes II: the narrowband phasing algorithm," Appl. Opt. **39**, 4706-4714 (2000).

[4] A. H. Bouchez *et al.*, "The Giant Magellan Telescope phasing system," Proc. SPIE **8447**, 84473S (2012).

[5] J. Codona, "Pairwise segment phasing with the GMT", GMT internal report (2008).

[6] S. Kanneganti *et al*, "A prototype phasing camera for the Giant Magellan Telescope," Proc. SPIE **8447**, 844752 (2012).

[7] Fang Shi *et al.*, "Experimental verification of dispersed fringe sensing as a segment phasing technique using the Keck telescope," Appl. Opt. **43**, 4474-4481 (2004).

[8] M. Albanese *et al.*, "Verification of the James Webb Space Telescope Coarse Phase Sensor Using the Keck Telescope," Proc. SPIE **6265**, 62650Z (2006).

[9] M. A. van Dam, B. A. McLeod and A. .H. Bouchez, "A Dispersed Fringe Sensor for the Giant Magellan Telescope," *to appear in* Applied Optics (2016).

[10] Gilbert Strang, *Linear algebra and its applications, 2nd edition*, Harcourt Brace, Florida, p. 138 (1980).

[11] F. Rigaut and M. van Dam,"Simulating Astronomical Adaptive Optics Systems Using Yao," AO4ELT3, 13173 (2013).

[12] M. A. van Dam *et al.*, "Modeling the adaptive optics systems on the Giant Magellan Telescope," SPIE Astronomical Telescopes+ Instrumentation, 773642 (2010).

[13] R. Conan *et al.*, "The Giant Magellan Telescope laser tomography adaptive optics system," Proc. SPIE **8447**, 84473P (2012).

[14] M. A. van Dam *et al.*, "Wide field adaptive optics correction for the GMT using natural guide stars," Proc. SPIE **9148**, 914813 (2014).

[15] M. S. Goodwin, "Turbulence profiling at Siding Spring and Las Campanas Observatories," Ph.D. Thesis, Australian National University (2009).

[16] G. Finger *et al.*,"SAPHIRA detector for infrared wavefront sensing," Proc. SPIE **9148**, 914817 (2014).

[17] D. Atkinson *et al.*, "Observatory deployment and characterization of SAPHIRA HgCdTe APD arrays," Proc SPIE **9154**, 915419 (2014).

[18] A.H. Bouchez, "Photometry for AO simulations," GMT internal document, GMT-02274, Rev 2.4 (2011).

[19] "Model of stellar population synthesis of the Galaxy," http://model.obs-besancon.fr.